Experiments in Fluids 32 (2002) 570–579 © Springer-Verlag 2002
DOI 10.1007/s00348-001-0400-9

The correlation between surface temperature and subsurface velocity during evaporative convection

J. R. Saylor, K. A. Flack, M. P. Schultz, G. B. Smith

Abstract The cross-correlation between surface temperature and subsurface velocity is presented for water undergoing evaporative convection. The surface temperature measurements were obtained via quantitative infrared imaging, and the velocity measurements were obtained using a two-component laser Doppler velocimetry (LDV) system. The water surface was covered with a surfactant monolayer, which did not impede evaporation. The largest measured correlation coefficient was 0.375. Correlation coefficients obtained after shifting the velocity and temperature time traces with respect to each other revealed a peak in the correlation coefficient very close to a zero time shift. The significance of these results and their implications for the remote sensing of underwater objects via infrared imaging are discussed.

1 Introduction

Evaporative convection is the natural convection that exists in a fluid layer bounded from above by a free surface that is experiencing evaporation and from below by a solid boundary (Berg et al. 1966). When the bottom boundary is insulated, evaporative convection is a form of unsteady nonpenetrative natural convection, since the average temperature of the layer is constantly changing (Adrian et al. 1986). The application to oceans, lakes, and rivers, where evaporation-driven flows naturally occur is obvious. Evaporative convection can also be related to the planetary boundary layer, where heat via solar influx is introduced at the bottom boundary and the top boundary is essentially insulated. This condition is exactly inverted, but analogous to evaporative convection. The one caveat to this analogy is that the surface where heat transfer occurs is solid in the planetary boundary layer case, while for evaporative convection, heat is transferred at a free surface.[1]

In this work velocity and temperature are measured in an evaporative convection flow. Temperature measurements are obtained at a point on the water surface, and velocity measurements are obtained at locations beneath this point. The degree of correlation between these velocity and temperature measurements is investigated. As described above, investigations of evaporative convection find application in various geophysical flows. Moreover, these correlations provide information on basic turbulence, of which evaporative convection is an example. However, the prime motivation for the experiments presented here is the remote detection of subsurface obstacles, such as mines.

The presence of an object beneath a water surface modifies any flow that exists beneath that surface. This change in the subsurface flow also alters the surface temperature field. Infrared imaging can be used to measure changes in the temperature field of a water surface, thereby providing a method for detecting submerged objects, such as mines. This is true even if the submerged object is in thermal equilibrium with the surrounding water.

The location of submerged mines has traditionally been achieved by any of several acoustic detection schemes. While successful, these methods require a dedicated asset located in the region of interest. This puts military personnel at risk, and in civilian applications such as bathymetric measurements, this method is costly and time consuming. A remote method for underwater detection is highly desirable.

Recent research has demonstrated that under some conditions, passive infrared (IR) detection of submerged mines is possible. Smith and Leighton (2001) investigated the surface temperature field in a water tunnel flow where a 12.7-cm sphere was submerged with the center of the sphere located 10 cm beneath the water surface. With a water speed of 23 cm/s and a wind speed ranging from 1.5 to 4 m/s, vortices that were shed from the sphere impinged on the water surface. These vortices were visible in the IR imagery as hot spots of fluid located just downstream of

Received: 2 April 2001/*Accepted*: 30 November 2001

J. R. Saylor (✉)
Clemson University, 229 Fluor Daniel Building
Box 340921, Clemson, SC 29634-0921, USA
e-mail: jrsaylor@ces.clemson.edu

K. A. Flack, M. P. Schultz
United States Naval Academy
Annapolis, MD 21402, USA

G. B. Smith
Naval Research Laboratory
Code 7253, 4555 Overlook Ave SW
Washington, DC 20375, USA

Financial support from the Office of Naval Research through the Naval Research Laboratory, and from the United States Naval Academy is gratefully acknowledged.

[1]The study herein concerns a liquid layer having a surfactant monolayer at the free surface, creating a constant elasticity boundary condition, which, as demonstrated by Handler et al. (1998), can give results that are, for some flows, indistinguishable from a no-slip boundary condition. Hence, this caveat is not as significant as might otherwise be the case.

the sphere. Although the IR imagery was somewhat complicated by the presence of wind, water flow, and waves, the strength of the vortex shedding from the sphere resulted in an IR signature on the water surface that was easily visible.

The method described above will work as long as there is an existing liquid flow that the submerged object can alter. In this work we consider the case where the subsurface flow is very weak. Specifically, we investigate a case where the only liquid motion is due to natural convection caused by evaporation at the water surface (evaporative convection), a zero-mean flow. Such situations are found, for example, in harbors or inlets where there is insignificant inflow from streams or rivers, and when the wind speed is zero. This condition represents the worst-case scenario (from the fluid mechanics perspective – other situations such as sunglint that complicate IR imaging must also be considered) for this mode of underwater detection.

Preliminary investigations of this condition were conducted by the authors in a glass tank containing a submerged glass sphere. Evaporation into a laboratory environment with no net air flow was the driving force for the flow. Infrared imaging of the water surface during these experiments resulted in imagery that did not reveal any obvious signature from the submerged sphere, even when the sphere was less than one diameter from the surface. However, when multiple images were processed to provide an average image, root-mean-square (rms) image, or skewness image, the presence of the submerged sphere was revealed as a spot in the center of this statistical image. An example of this is presented in Fig. 1a, where an instantaneous snapshot of the surface temperature field is presented and no evidence of the presence of the submerged sphere can be seen. In Fig. 1b an image of the skewness of 1500 images is presented, which reveals the presence of the submerged sphere. It is noted that the temperature fields presented in Fig. 1 are *surface* temperature fields; the camera is only sensitive to radiation emitted from the top 25 μm of the water column.

While the results presented in Fig. 1 are intriguing and seem to call for a detailed study of the relevant parameters (mine depth, humidity, and water velocity), a more fundamental initial investigation of the correlation between surface temperature and subsurface velocity is needed. Such a study provides a quantitative measure of exactly how much subsurface information is present at the water surface, putting this method on a firmer quantitative underpinning.

It should be noted that a microwave radar method for detecting submerged objects that is somewhat analogous to the one proposed here was demonstrated by Sletten (2000). In this work the presence of a broached and submerged mine-like object was detected via active microwave scattering. The detection method relied on flow disturbances that were strong enough to change the topology of the water surface downstream from the object. In the current work, we envision a mine detection environment that is much less welcoming, in that the flow is not strong enough to disturb the water surface topology. Another remote method for detecting submerged mines that is based on active laser scattering has been demonstrated (McLean and Freeman 1996; Vitsinskii et al. 1998). However, laser-based methods require water of low turbidity, a condition that is frequently violated in coastal areas, where shore runoff and surf zones can render the water opaque to visible radiation.

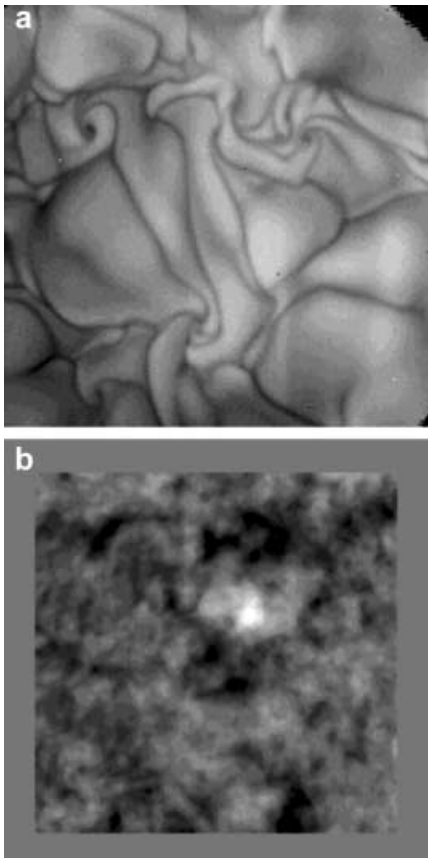

Fig. 1. Infrared images of a water surface undergoing evaporative convection. A glass sphere is located beneath the water surface. **a** An example of a single instantaneous snapshot. The black regions (*upper and lower right corners*) correspond to nonfunctioning camera pixels. **b** Skewness image obtained from 1500 images. The gray border was included to exclude the nonfunctioning pixels

2 Experimental method

The experimental facility used in these experiments is illustrated in Fig. 2, which shows the tank, the optical setup used to obtain laser Doppler velocimetry (LDV) measurements, and the location of the infrared camera. The tank is made of glass and is sealed using an RTV silicone sealant. This is the same tank that was used in our previous experiments (Saylor et al. 2000a, 2000b, 2001; Flack et al. 2001). Any indigenous surfactants on the glass walls or RTV seals are assumed to have been eliminated during the many deionized water flushes that were part of the cleaning procedure during the current and previous experiments. The dimensions of the tank are 30 cm by 30 cm by 15 cm deep. The tank is insulated on four sides to reduce heat loss.

The heat flux was measured using calorimetry. The bulk water temperature was measured using a teflon-coated

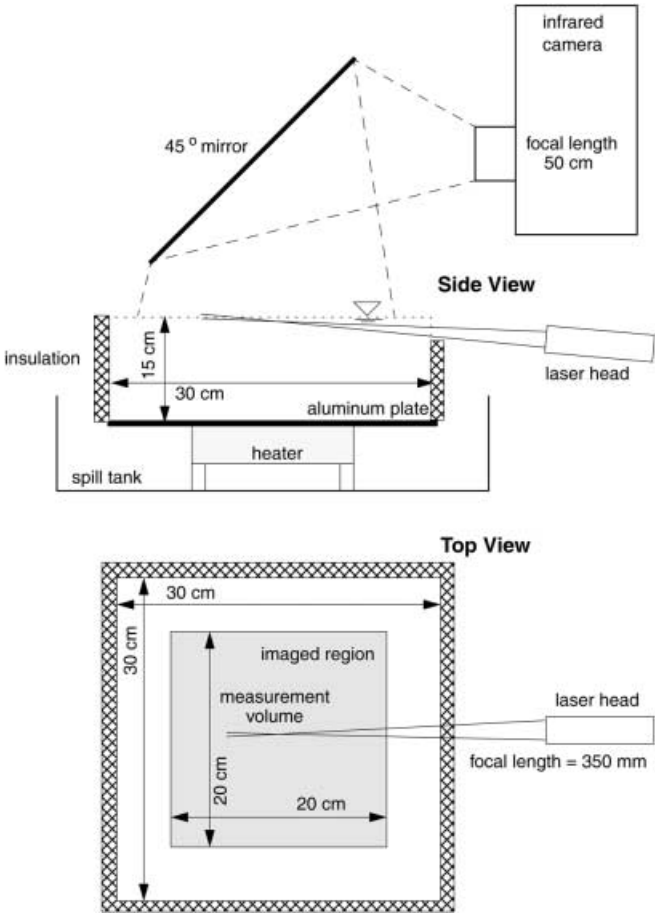

Fig. 2. Experimental setup for temperature–velocity correlations

thermocouple having a resolution of 0.1 °C, and the rate of temperature drop dT_b/dt, along with the surface area of the water, was used to compute the heat flux from the water surface. Heat transfer through the tank walls and floor was measured during a separate set of experiments, and these values were used to correct the values of heat flux reported here. To provide a larger infrared signal, the water was heated above the ambient air temperature to ~38 °C and allowed to cool to ~32 °C over a period of about 2 h, during which time ten experiments were conducted. Each group of ten experiments is referred to here as an experimental group. The process of cooling was accompanied by a reduction in heat flux. Typically, the heat flux dropped by ~180 W/m^2 during the course of all ten experiments in an experimental group. The starting and ending heat fluxes for each experimental group are presented in Table 1. It should be noted that during each experiment, data were acquired for only 500 s, during which time the variation in heat flux was on the order of 5%.

Deionized water was used in all experiments and for all cleaning procedures conducted prior to the experiments. The deionized water was obtained from a deionization system (Milli-Q UV Plus) consisting of a single distillation unit, followed by a millipore filter and an ultraviolet filter. Care was taken to avoid contamination by indigenous surfactants in all portions of the experimental procedure. The specific procedures used to prevent such contamination are presented in Saylor et al. (2000a).

Table 1. Values of starting heat flux, ending heat flux, and total length for each group of experiments. Ten experiments were conducted in each group

z (mm)	Experimental group number	Starting flux (W/m^2)	Ending flux (W/m^2)	Duration (min)
1.0	1	369	214	123
1.0	2	379	225	112
5.0	3	410	195	112
5.0	4	434	228	133
20.0	5	357	192	134
20.0	6	414	212	113

Prior to each experiment a surfactant monolayer was deposited on the water surface. Clean surfaces were not investigated in this study since the near-shore areas envisioned for the application of interest are most likely covered with some type of surfactant. The surfactant used was oleyl alcohol because its elasticity properties are similar to those of monolayers found on the ocean surface (Barger 1991). In addition, because oleyl alcohol does not impede evaporation (Katsaros and Garret 1982), investigation of evaporative convection was not hindered by the very low evaporation rates that would have been attained had an evaporation-impeding surfactant been used. The oleyl alcohol monolayer was deposited by spreading a stock solution of oleyl alcohol and HPLC-grade heptane. The solution quickly spread over the water surface (Saylor et al. 2000b), and upon evaporation of the heptane, left a monolayer of oleyl alcohol having a surface concentration of $c = 0.11$ μg/cm^2. Oleyl alcohol is insoluble in water; hence its concentration on the water surface was constant throughout the experiment.

The water surface temperature was obtained by IR imaging using an infrared camera (Raytheon-Amber AE4256 IR, Fig. 2) having a 256 × 254 InSb focal plane array and a 12-bit dynamic range. The camera is liquid nitrogen cooled and exhibits a noise level equivalent to approximately 25 mK in measured temperature. The water surface was imaged through a mirror oriented at 45°, and the imaged region was approximately 16 cm on a side. Calibration images were obtained after each set of experimental runs. These images were used to create calibrations relating pixel intensity to absolute temperature. Each pixel in each frame of the experimental data sets was converted to temperature using these calibrations.

As noted above, the water temperature decreased during the course of the experiments. Time traces were constructed from the infrared data by plotting the temperature at a single pixel against the time at which the frame was recorded. These time traces have a "tilt" or downward trend, due to the decreasing temperature of the water bulk. This decrease in temperature presents a problem when comparing temperature time traces to the velocity time traces, which do not exhibit such a tilt. To address this problem, the average frame temperature was subtracted from each frame. This eliminated the local (temporal) average from each point in the time trace, thereby "flattening" the traces.

Subsurface velocity was measured using a LDV system (TSI ColorBurst) using a 4-W argon-ion laser. As indicated

in Fig. 2, a laser head containing the transmitting and receiving optics for backscatter data acquisition was connected to the laser via a fiber-optic cable, which handled all four beams. A 350-mm focal length lens mounted in the laser head created a measurement volume having a length of 1.3 mm and a diameter of 0.09 mm. Since near surface measurements were the focus of this work, it was necessary to slightly tilt the laser head so that all four laser beams could enter the tank without interference from the meniscus. The axes of the four laser beams are located on the four corners of a square. The normal setup for this system requires that the lines connecting opposing corners of this square be parallel to the velocity components of interest. However, a reduced angle of tilt for the laser head was achieved by rotating the head 45° from the normal orientation. This 45° rotation necessitated a coincidence sampling of the two channels, since velocity information is mixed between channels in this configuration. Subsequent coordinate transformation was used to find the horizontal component of velocity u and the vertical component of velocity v. The coincidence window was set at 0.01 s.

The water was seeded with neutrally buoyant hollow glass spheres, approximately 10 μm in diameter. Measurements at high data rates proved challenging because of the low velocities, which were on the order of 1 mm/s for both components. The fringes were shifted at 5 kHz to remove directional ambiguity. The resulting fringe velocity of approximately 18 mm/s resulted in multiple readings when slow-moving particles entered the measurement volume. The repeated validations for such particles were filtered from the data using a minimum time between valid bursts.

The goal of these experiments was to determine the degree of correlation between the surface temperature and the subsurface velocity for velocities measured at different depths beneath the surface. Three depths were investigated, $z = 1$, 5, and 20 mm. At each depth, 20 experimental runs (two experimental groups per depth, Table 1) were conducted. Each run lasted 500 s, during which time velocity and temperature data were simultaneously recorded. The LDV system provided time traces of u and v. To obtain the corresponding time traces of temperature θ, it was necessary to locate the pixel in the IR image whose position in x–y-space was directly above the LDV measurement volume. This was achieved by placing the corner of a cool Plexiglas plate immediately over the LDV measurement volume. This plate appeared as a very dark object in the IR image, and the corner was easy to locate. The x–y-location of this corner was recorded, and a temperature time trace was constructed by extracting the value of this pixel from each frame. Because the characteristic structures in the IR data were large relative to the pixel size, binning pixels in space to reduce noise was an option. A 2×2 binning was tested, and the results were indistinguishable from those obtained using a single pixel. Only single-pixel extraction results are presented here.

The correlation of temperature θ and velocity U was quantified using the correlation coefficient, defined as

$$\rho = \frac{\overline{\left(\theta(t) - \bar{\theta}\right)\left(U(t) - \bar{U}\right)}}{\sigma_\theta \sigma_U} \quad , \tag{1}$$

where U is either component of velocity u or v, $\overline{\theta}$ is the average temperature, $\overline{U}$ is the average velocity (again for either u or v), and σ_θ and σ_U are the standard deviations of temperature and velocity, respectively. The sampling rate for the infrared camera was 1 frame/s, resulting in a 1-Hz data rate for the θ trace. The sampling rate and number of data points in the velocity trace varied because of the inherent nature of the LDV method. However, it was always much faster than the temperature data rate (on the average, each 500-s velocity trace contained ~18,000 valid data points). The numerator in (1) is computed by multiplying each point in the θ time trace with the point in the U time trace that occurs at the same instant in time. Because U was sampled more frequently than θ, the computation of ρ involved visiting each point in the θ time trace and then searching the U time trace for the closest point in time to that θ point. When the closest point in the U trace happened to be more than 0.3 s away from the corresponding point in the θ trace, this point was rejected and was not used in computing the correlation coefficient. This typically resulted in a rejection rate of 30%. The 0.3-s threshold was deemed sufficiently small due to the relatively slow change in the temperature time trace, (Fig. 3).

3 Results

Time-traces for θ and v for a sample experimental run are presented in Fig. 3. Local regions where θ and v are correlated can be seen. For example, both traces exhibit a sharp peak near t~120 s. The peak in v, however, occurs slightly ahead of the peak in θ. Because the velocity probe is located beneath the surface, it is possible that events may be observed in one trace before or after they are observed in the other. Therefore, instead of computing a single correlation coefficient for each case, we progressively shift one trace with respect to the other to provide a range of correlation coefficients. This is achieved by modifying (1) to give:

$$\rho = \frac{\overline{\left(\theta(t) - \bar{\theta}\right)\left(U(t + \Delta t) - \bar{U}\right)}}{\sigma_\theta \sigma_U} \quad , \tag{2}$$

where Δt can be positive or negative. Plots of ρ versus Δt are presented in Figs. 4–6 for each of the three depths investigated. The u–θ and v–θ correlations, $\rho_{u\theta}$ and $\rho_{v\theta}$, respectively, are presented in each plot. For all three cases, $\rho_{v\theta}$ displays a peak. The peak correlations and the value of Δt at which they occur are presented in Table 2.

For all three depths $\rho_{u\theta}$ is small. There is the appearance of a slight peak in $\rho_{u\theta}$, however, it is small and barely exceeds the noise in the plots.

In several of the plots, the noise superimposed on the ρ versus Δt data has a periodic structure with frequency of ~1 Hz. This is caused by the spacing of data points in the θ trace, which were obtained at 1-s intervals. At a given value of Δt, only velocity data points that are close in time to the θ points are used, in accordance with the computational scheme described in Sect. 2. If Δt is increased by exactly 1 s, the same set of velocity points are used in computing ρ. Although they will be multiplied by different θ points, any anomalies in the set will be reflected in the ρ

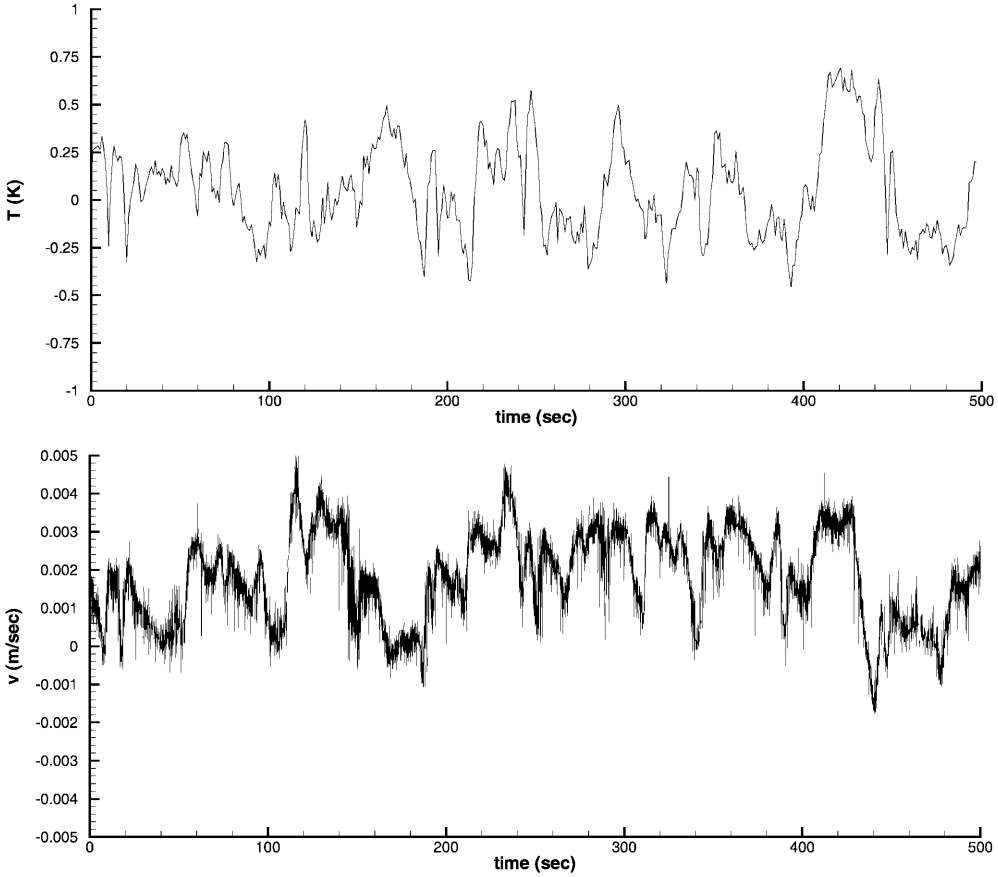

Fig. 3. Sample time traces for θ and v. The velocity measurement volume is located at depth $z = 5$ mm

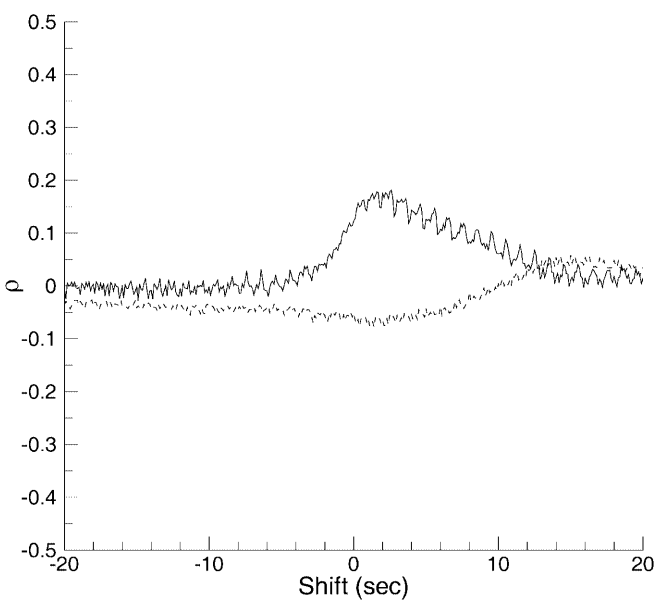

Fig. 4. Plots of θ–u (*dashed line*) and θ–v (*solid line*) correlation at $z = 1$ mm as a function of the time shift Δt between the temperature and velocity signals

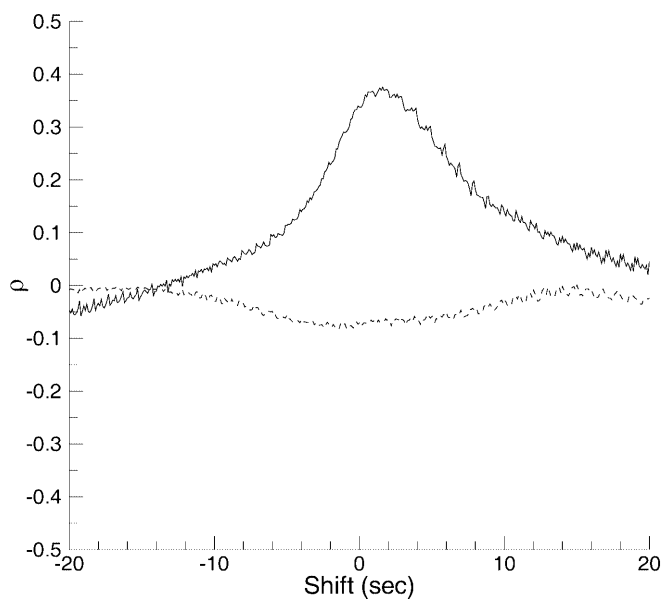

Fig. 5. Plots of θ–u (*dashed line*) and θ–v (*solid line*) correlation at $z = 5$ mm as a function of the time shift Δt between the temperature and velocity signals

versus Δt plots and will recur at 1-s intervals, creating the 1-Hz noise observed in the ρ versus Δt plots.

Finally, in Figs. 7 and 8, scatter plots of θ versus u and θ versus v are presented for all three cases investigated. These plots are constructed for a zero time shift between the θ and U traces, i.e. $\Delta t = 0$. The θ versus u plots display a pattern that is very circular, as is expected from the small values of $\rho_{u\theta}$ presented in Figs. 4–6. For the θ versus v scatter plots, the positive correlation is evident in the eccentricity of the pattern, oriented along a line running between quadrants 3 and 1, particularly in Fig. 8b. Careful

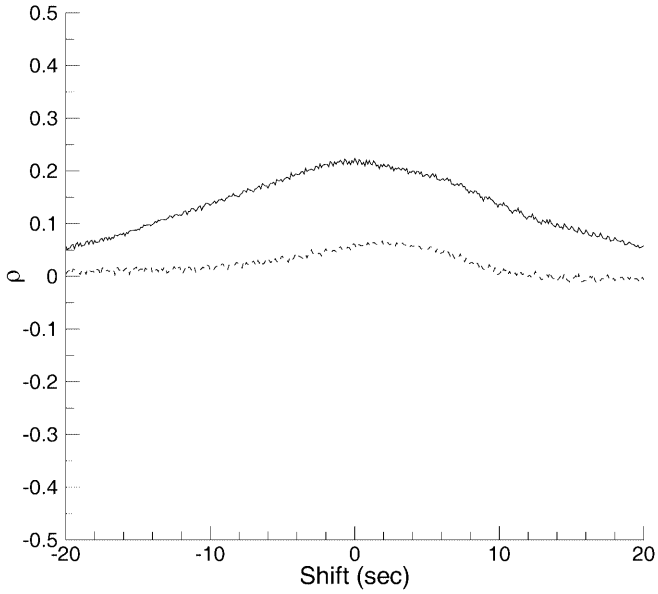

Fig. 6. Plots of θ–u (*dashed line*) and θ–v (*solid line*) correlation at $z = 20$ mm as a function of the time shift Δt between the temperature and velocity signals

Table 2. Peak values for the v–θ correlations at each of the three depths investigated. The Δt at which the peak was located is included

z (mm)	Peak v–θ correlation	Δt (s)
1.0	0.181	2.6
5.0	0.375	1.6
20.0	0.224	0.0

observation of the scatter plots reveals a lack of symmetry when the data is projected on the velocity axis for the θ versus v plots. The significance of this is discussed in Sect. 4, where probability density functions (pdfs) of v are presented.

4 Discussion

The primary goal of this work was to ascertain the degree of correlation between surface temperature and subsurface velocity during evaporative convection. The results presented in Table 2 reveal that, to a depth of 20 mm, significant, measurable correlations exist between the surface temperature and the vertical component of velocity. To the authors' knowledge, these are the first measurements of correlation coefficients for evaporative convection.

The mechanism responsible for the significant positive correlation coefficients that were observed is now discussed. In general, it would be reasonable to attribute the correlation between temperature and velocity to simple turbulent transport. Two observations suggest that this is probably not the case here. First, as indicated in Table 2, the Δt at which the peak value for $\rho_{v\theta}$ is observed is small. At a depth of 20 mm, the peak is located at $\Delta t = 0$ s. Although noise in the data may obscure a peak that differs slightly from zero, it certainly is not significantly different from ±1 s. The magnitude of the velocity fluctuations in

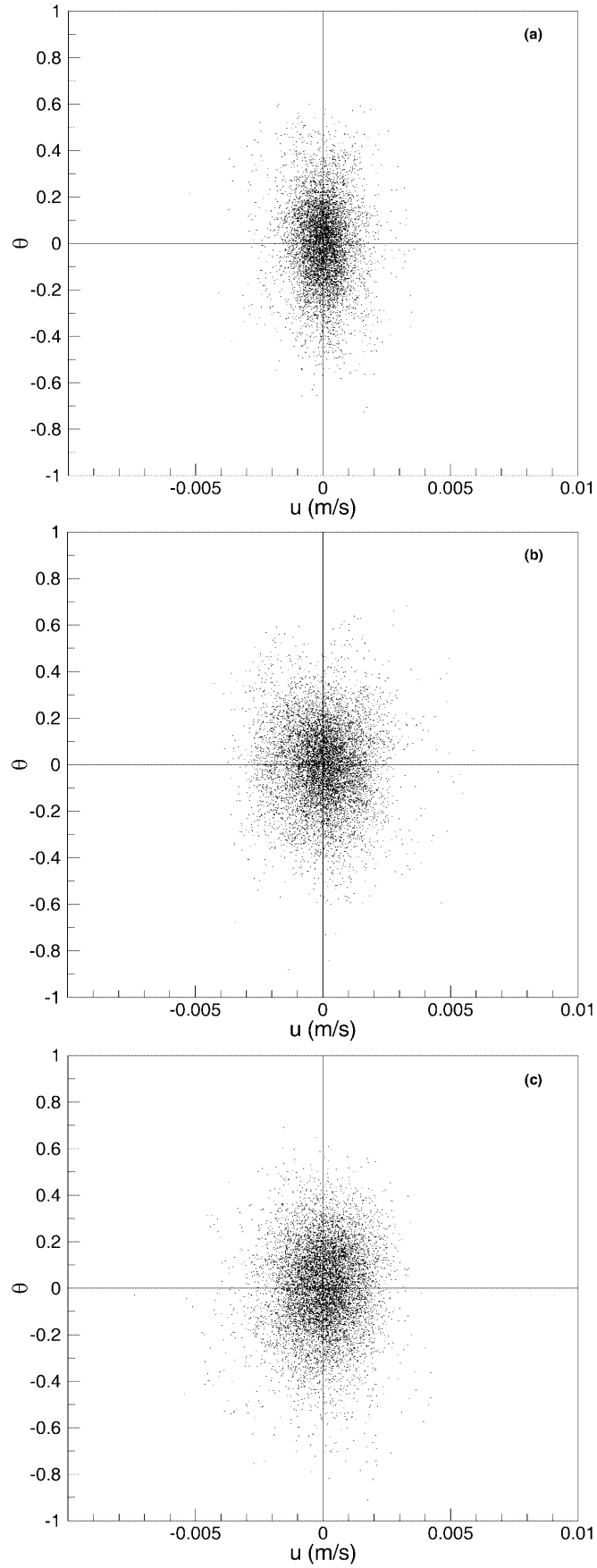

Fig. 7a–c. Scatter plots of θ versus u: **a** $z = 1$ mm; **b** $z = 5$ mm; **c** $z = 20$ mm

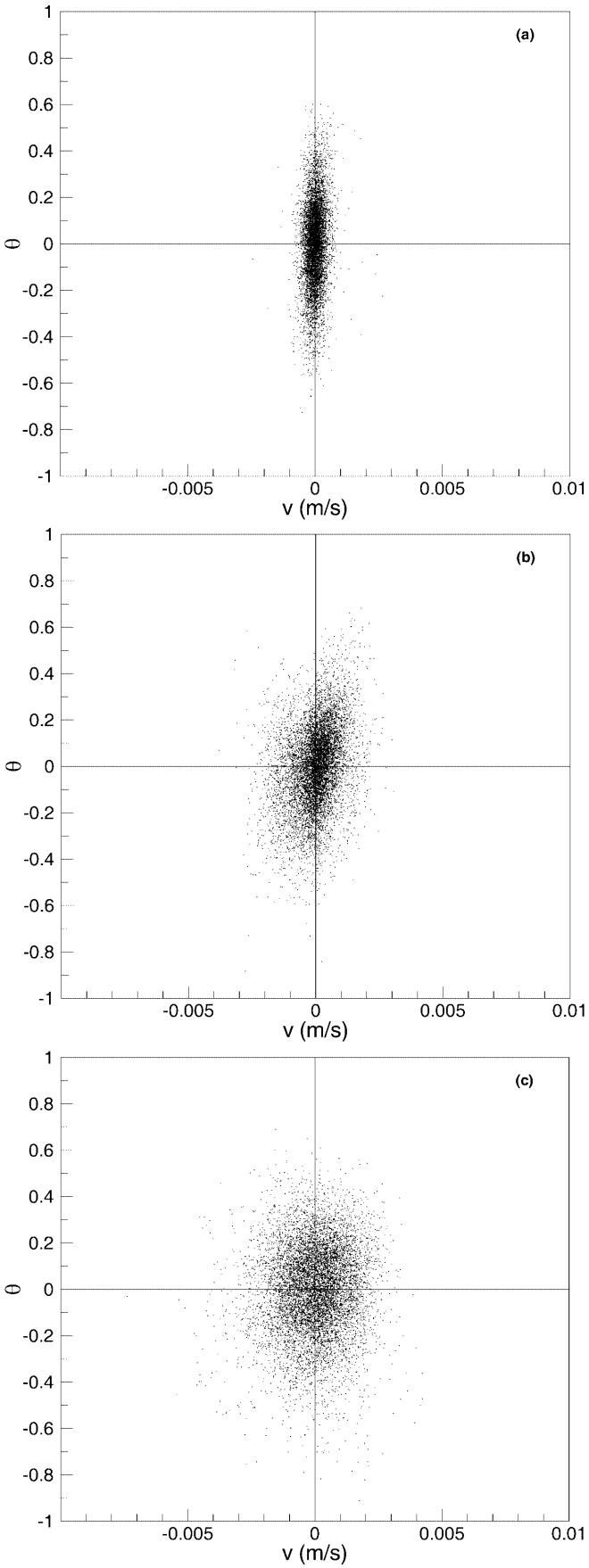

Fig. 8a–c. Scatter plots of θ versus v: **a** $z = 1$ mm; **b** $z = 5$ mm; **c** $z = 20$ mm

these experiments was on the order of 1 mm/sec. Hence, an event occurring at a depth of 20 mm would require a delay on the order of 20 s to reach the water surface via turbulent transport. Since this is not the case, an alternative explanation for the magnitude of the correlations obtained is sought.

Several researchers have noted that the large-scale flow observed in evaporative convection consists of thin, falling sheets with relatively large velocities, interspersed with larger rising plumes with smaller velocities (Volino and Smith 1999; Spangenberg and Rowland 1961; Katsaros et al. 1977; Foster 1965). These structures remain coherent for a significant distance. Flow visualizations found by Katsaros et al. (1977) displayed a falling sheet that extended from the water surface to a depth of 40 mm, the edge of the visualized regions. This visualization was obtained at a heat flux of 270 W/m^2, not dissimilar from the heat fluxes measured here. Spangenberg and Rowland (1961) observed falling sheets that reached the bottom of their water tank, which was 100-mm deep. Heat fluxes were not reported. Volino and Smith (1999) obtained velocity fields perpendicular to the water surface using particle image velocimetry (PIV). In a low-heat-flux experiment (60 W/m^2), the authors present a velocity field revealing what appears to be a falling sheet structure, penetrating to a depth of at least 80 mm (the edge of the measured field). Taken in total, these studies suggest that in the present work, falling sheets penetrating to the deepest measurement depth of 20 mm should not be uncommon.

Such falling sheets with interspersed rising plumes can explain the *magnitude* of the correlations reported in Table 2. A rising plume brings warm fluid to the surface (positive velocity, positive temperature fluctuation), while a falling sheet thickens the boundary layer, cooling the surface (negative velocity, negative temperature fluctuation). However, such falling sheets and rising plumes are traveling at speeds that are, again, on the order of 1 mm/s in the vertical direction. How such structures can be responsible for the small value of Δt at which the peak correlation is observed in Figs. 4–6 requires additional explanation.

Observation of the structures present in the IR imagery indicates that the dark (cold) lines on the water surface, from which the falling sheets evolve, are translated significant distances across the surface before they disappear. In other words, for relatively long periods of time, the falling sheets remain coherent and are laterally translated about the tank. This is most easily observed in the IR imagery when presented as a movie, but can also be seen in Fig. 9, where four images are presented, each obtained 20 s apart. The spiral structure seen in the lower right corner of Fig. 9a moves in the vertical direction from frame to frame, without changing significantly. Hence over a period of 1 min, this structure remains coherent. As such structures pass over the LDV and IR measurement location, a sudden change in velocity and temperature should simultaneously be observed by both detectors. Hence, a positive correlation is created, without a delay between the two observed signals. Of course, this assumes that the falling sheet remains oriented in a vertical fashion, while

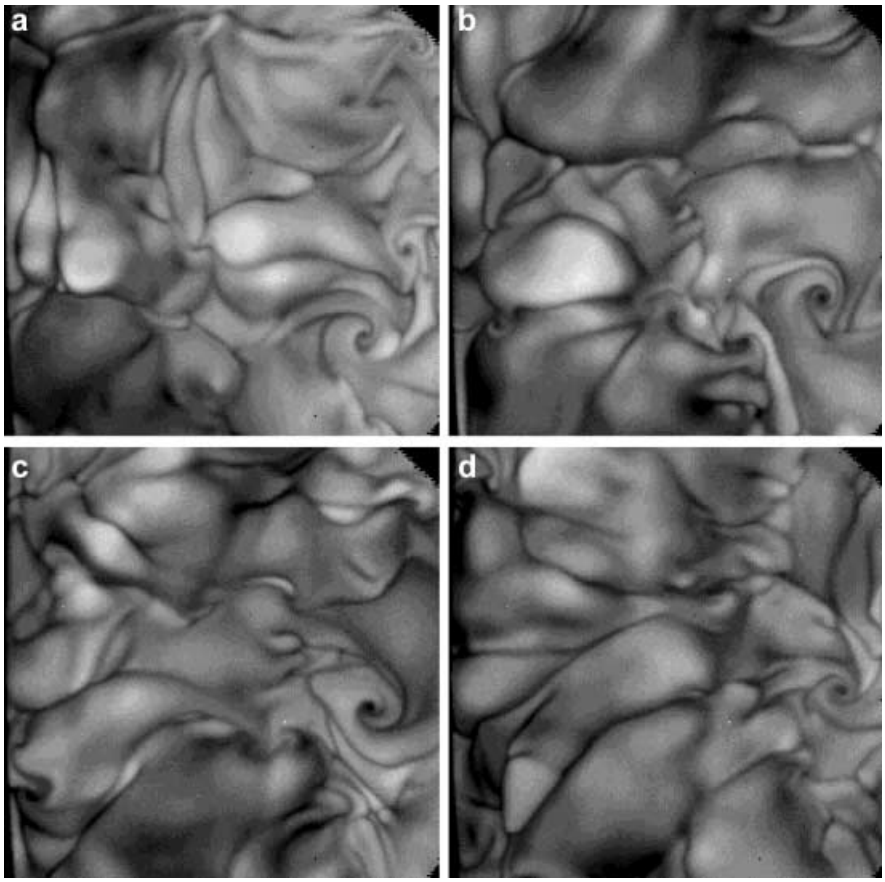

Fig. 9a–d. Temperature fields of images spaced 20 s apart. Dark regions (*upper and lower left corners*) correspond to non-functioning pixels

some of the sheets may in fact be tilted. However, in this case, the small value of Δt at which the peak correlation occurs in Figs. 4–6 would still be observed. Some of the sheets would be tilted in one direction, and others in the opposite direction, averaging out to a zero value for the location of Δt in these plots.

As noted earlier, a significant correlation between v and θ is observable at the maximum depth investigated, here 20 mm. One of the motivations of this work was a desire to predict how IR imagery might be used to locate submerged objects. Accordingly, it is useful to relate the depths investigated here to the corresponding depths in a harbor or near-shore environment. This is difficult to do, since scaling arguments for the correlation coefficient of the type presented here have not appeared in the literature. Nevertheless, a crude relation can be made. The experiment conducted here is a type of nonpenetrative convection. Scaling arguments for the moments of temperature and velocity fluctuations, as well as for *local* correlations between the two have been developed by several authors (Adrian et al. 1986; Sorbjan 1990; Prasad and Gonuguntla 1996) for nonpenetrative convection. These authors have shown that such quantities collapse when plotted as a function of z/z_*, where z_* is the total fluid depth. For the current experiment, z_* is the tank depth, 15 cm. For a harbor or near-shore region, z_* would be either the ocean depth, or the depth at which the vertical flux of heat is sufficiently close to zero that an insulated condition can be assumed. Assuming that $\rho_{v\theta}$ scales as the local correlation between temperature and velocity (i.e. the correlation between the temperature and velocity when both are measured at the same location), for the deepest measurement location $z/z_* = 0.13$. Hence for a harbor of, say, 20-m depth, the $z = 20$ mm case considered here would correspond to a depth of 2.6 m, indicating that objects submerged a fairly significant distance may be detectable via passive IR imaging. This analysis ignores effects such as wind or mean water currents. However, as noted in Sect. 1, such effects are likely to improve the detectability of submerged objects via IR imagery.

Although measurements were only obtained at three depths, some discussion of the behavior of $\rho_{v\theta}$ versus z is warranted. The smallest value for $\rho_{v\theta}$ (Table 2) is found at a depth of 1 mm. Moving from $z = 1.0$ mm to 5.0 mm, $\rho_{v\theta}$ increases to the maximum value observed in these experiments, 0.375, and drops to 0.224 at a depth of 20 mm. With only three depths investigated, a peak at 5.0 mm cannot be used to demonstrate a local maximum, and further experiments would be necessary to determine where such a maximum lies. The decrease in $\rho_{v\theta}$ as the depth decreases from 5.0 mm to 1.0 mm is curious. One would expect a correlation coefficient between two signals to increase as the distance between their measurement locations decreases. Because v decreases as $z \to 0$, part of the reason may simply be that σ_v in (1) is influenced by noise at $z = 1.0$ mm. A more plausible explanation, however, can be found in the work of Volino and Smith (1999), where velocity fields were obtained near the surface of water undergoing evaporative convection. In the velocity field presented in their Fig. 6, a falling sheet is clearly

visible 4–8 cm beneath the surface. However, in the region closer to the surface (yet still above this falling sheet), the velocity field appears more random and does not exhibit a clear downward flow trend. It seems, in this case at least, that the falling sheet is the result of an instability that is only fully manifest at some finite distance beneath the surface. These results suggest that the falling sheets, which create the low temperatures on the water surface, only fully express themselves in the velocity field at some finite depth beneath the surface, explaining the decrease in $\rho_{v\theta}$ as z is reduced from 5.0 mm to 1.0 mm. It is noted in passing that both the numerator and denominator of (1) approach zero as $z \rightarrow 0$. Hence, there will be some limiting behavior for $\rho_{v\theta}$ in the limit of small z. Further experiments where $\rho_{v\theta}$ is obtained at finely spaced intervals of z, near the surface, are required to determine this behavior.

The primary motivation of this work is the detection of submerged objects by observing changes in the surface temperature field. Such changes occur when disturbances of the subsurface flow caused by the object impinge upon the surface and alter the temperature field. The positive correlation between temperature and velocity reported here suggests that detection schemes based on this principal should work. However, it must be noted that it is the rising plumes that most directly communicate the presence of a submerged object to the surface temperature field. A submerged object disturbs the upward flow of a plume, thereby changing the surface temperature field. The positive correlations measured here result from both the rising plumes and falling sheets, yet only the plumes directly provide information about subsurface events. Since the sheets and plumes are intimately tied together (the sheets feed the plumes), a positive value of $\rho_{v\theta}$ still indicates that information about a submerged object can be obtained from the surface temperature field. Nevertheless, it would be interesting to compute $\rho_{v\theta}$ using only data points where v is positive. This is left as future work.

A final point of interest concerns the distribution of the vertical velocity component. As discussed above, flow visualizations have revealed that the subsurface flow during evaporative convection is comprised of thin falling sheets and larger rising plumes. By necessity of conservation of mass, the sheets must have a larger velocity magnitude than the plumes. From a statistical perspective, this means that a large negative value of v is more probable than a large positive value, or stated another way, the skewness for v should be negative. In Fig. 10, the pdf of v is presented for each of the three depths investigated. Contrary to expectation, the pdf for $z = 1$ mm is actually slightly positively skewed, while, as expected, negative skewness is observed at $z = 5$ mm and $z = 20$ mm. The work of Volino and Smith (1999) may explain this result. In their Fig. 7, plots of the vertical component of velocity against the horizontal direction are presented for depths of 5.7, 11.5, and 40.3 mm, all obtained at the same instant in time. The two measurement locations nearest the surface reveal a seemingly symmetric distribution of positive and negative components of velocity. However, at a depth of 40.3 mm, a large thin region is observed that has a large negative velocity and is surrounded by broad areas having

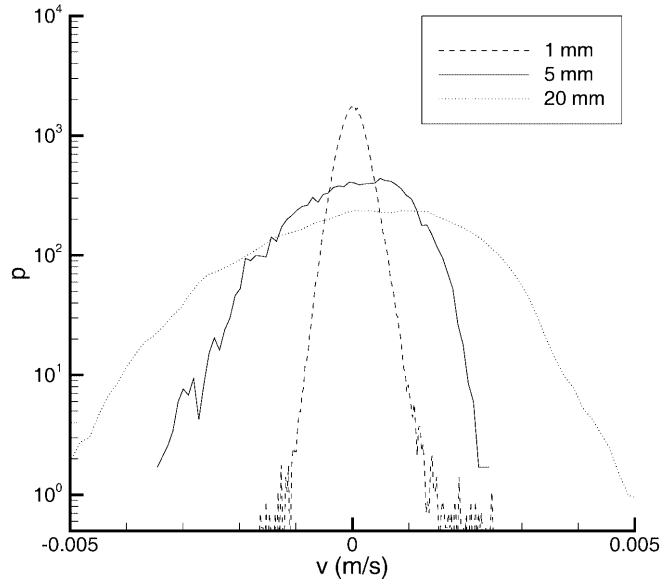

Fig. 10. Probability density functions of v

a small positive component of vertical velocity. These results coupled with those presented here seem to indicate that during evaporative convection, structures consisting of thin falling sheets and large rising plumes do indeed exist. However, these thin falling sheets seem to form not at the very surface of the water, but perhaps by consolidating smaller falling parcels of falling fluid into one larger falling sheet.

5 Conclusion

Measurements of the correlation coefficient of subsurface velocity and surface temperature θ for evaporative convection revealed significant correlation for heat fluxes in the range 192–434 W/m^2. A peak value of 0.375 for the correlation of θ and the vertical component of velocity was measured at a depth of 5 mm. Correlations between θ and the horizontal component of velocity were close to zero. The existence of falling sheets and rising plumes observed by other researchers can explain several aspects of these results. The magnitude of the measured correlations lends credence to the viability of passive IR imaging as a tool for locating submerged objects.

References

Adrian RJ; Ferreira RTDS; Boberg T (1986) Turbulent thermal convection in wide horizontal fluid layers. Exp Fluids 4: 121–141

Barger WR (1991) A review of experimental observations and remaining questions concerning formation, persistence, and disappearance of sea slicks. NRL Report 9313, Naval Research Laboratory, Washington, DC, pp 1–46

Berg JC; Acrivos A; Boudart M (1966) Evaporative convection. In: Drew TB; Hoopes JW; Vermeulen T (eds) Advances in Chemical Engineering, vol 6. Academic Press, New York, pp 61–124

Flack KA; Saylor JR; Smith GB (2001) Near-surface turbulence for evaporative convection at an air/water interface. Phys Fluids 13: 3338–3345

Foster TD (1965) Onset of convection in a layer of fluid cooled from above. Phys Fluids 8: 1770–1774

Handler RA; Smith GB; Leighton RI (1998) Vortex interactions with a thermal boundary layer at a surfactant contaminated

free surface. In: Proceedings of ASME Fluids Engineering Division Summer Meeting, Washington, DC, 21–25 June
Katsaros KB; Garrett WD (1982) Effects of organic surface films on evaporation and thermal structure of water in free and forced convection. Int J Heat Mass Trans 25: 1661–1670
Katsaros KB; Liu WT; Businger JA; Tillman JE (1977) Heat transport and thermal structure in the interfacial boundary layer measured in an open tank of water in turbulent free convection. J Fluid Mech 83: 311–335
McLean JW; Freeman JD (1996) Effects of ocean waves on airborne lidar imaging. Appl Optics 35: 3261–3269
Prasad AK; Gonuguntla PV (1996) Turbulence measurements in nonpenetrative thermal convection. Phys Fluids 8: 2460–2470
Saylor JR; Smith GB; Flack KA (2000a) The effect of a surfactant monolayer on the temperature field of a water surface undergoing evaporation. Int J Heat Mass Trans 43: 3073–3086
Saylor JR; Smith GB; Flack KA (2000b) Infrared imaging of the surface temperature field of water during film spreading. Phys Fluids 12: 597–602
Saylor JR; Smith GB; Flack KA (2001) An experimental investigation of the surface temperature field during evaporative convection. Phys Fluids 13: 428–439
Sletten MA (2000) Ultra-wideband radar images of the surface disturbance produced by a submerged mine-like object. IEEE Trans Geosci Remote Sensing 38: 2506–2514
Smith GB; Leighton RI (2001) Infrared detection of the disruption of the thermal boundary layer at an air–water interface by a subsurface wake. Exp Fluids, in press
Sorbjan Z (1990) Similarity scales and universal profiles of statistical moments in the convective boundary layer. J Appl Meteorol 29: 762–775
Spangenberg WG; Rowland WR (1961) Convective circulation in water induced by evaporative cooling. Phys Fluids 4: 743–750
Vitsínskiĭ SA; Divin VD; Lovchiĭ IL; Keller AV (1998) Laser radiation for probing a water medium. J Opt Technol 65: 505–507
Volino RJ; Smith GB (1999) Use of simultaneous IR temperature measurements and DPIV to investigate thermal plumes in a thick layer cooled from above. Exp Fluids 27: 70–78